Effect of Robin boundary conditions on the onset of convective torsional flows in rotating fluid spheres

J. Sánchez Umbría* and M. Net†

Physics Department, Universitat Politècnica de Catalunya,

Jordi Girona Salgado 1–3, Campus Nord,

Mòdul B4, 08034 Barcelona, Spain

(Dated: October 9, 2023)

Abstract

Torsional flows are preferred at the onset of thermal convection in fluid spheres with stress-free and perfectly conducting boundary conditions, in a narrow region of the parameter space for Prandtl numbers $\mathrm{Pr} \lesssim 0.9$ and ratios $\mathrm{Pr}/\mathrm{Ek} = \mathcal{O}(10)$, Ek being the Ekman number. In this case the transport of heat to the exterior is supposed instantaneous. When the thermal conductivity of the internal fluid is large, and the external convective heat transfer or radiative emissivity are low, the heat transmission is less efficient, and the thermal energy retained in the interior increases, enhancing the onset of convection. This study is devoted to analyze the combined influence of the thermal conductivity and external conditions (temperature and resistance to heat transport) on the onset of the torsional convection by taking a Robin boundary condition for the temperature at the surface of the sphere. It is shown, by means of the numerical computation of the curves of simultaneous transitions to torsional flows and Rossby waves, that when the heat flux through the boundary decreases the region where the axisymmetric flows are preferred shrinks, but it never strangles to an empty set. It has been found that with adequate scalings the curves delimiting the transition to torsional flows, and those of the critical Rayleigh number, Ra_c, and the frequencies of the modes versus Ek become almost independent of the parameter of the Robin boundary condition.

PACS numbers: 47.15.-x, 47.20.-k

Keywords: Hydrodynamic stability, Rotation, Thermal convection, Boundary conditions, Bifurcations, Symmetry breaking

* juan.j.sanchez@upc.edu; Corresponding author.

† marta.net@upc.edu

I. INTRODUCTION

Knowledge of the purely inertial and thermal inertial flows in rotating fluid spheres, spherical shells, and spheroidal objects, is fundamental for the understanding of the dynamics of the fluid celestial bodies. Large-scale patterns can be recognized in many planets and in the Sun despite being mainly turbulent. Therefore, solving hydrodynamic stability problems is very useful to determine the nature of some observed astrophysical phenomena. For instance, the inertial modes obtained solving an eigenvalue problem for a fluid shell with stress-free boundaries [1] have been successfully compared with the equatorially antisymmetric retrograde propagating vorticity waves detected in the Sun from helioseismic and correlation-tracking analyses of ground- and space-based observations [2].

The number of approximations that define each problem is large, as well as the number of parameters, and boundary conditions that can be selected, so that the fluid dynamics can be diverse depending on these factors. The most common preferred eigenfunctions at the onset of Boussinesq and anelastic thermal convection in spherical geometry give rise to azimuthal rotating waves (ARWs). This is so with combinations of either non-slip [3–7], stress-free [8–10] or mixed [11] boundary conditions for the velocity field, together with either perfectly conducting [10], fixed heat flux through the boundaries [10, 12], Robin [11], or even laterally varying [13] boundary conditions for the temperature. The eigenfunctions break the invariance by rotation of the conduction state, but maintain the reflection symmetry with respect to the equatorial plane. Equatorially antisymmetric modes were first found to be preferred in a spherical shell of radius ratio $\eta = 0.4$ at small Ekman, Ek, and Prandtl, Pr, numbers under both non-slip and stress-free, and constant temperature boundary conditions [14]. More recently they were also found in thin shells [15]. In the first case the equatorial symmetry is maintained even when the flow is quasiperiodic, see for instance [16, 17] among many others. In the second, the antisymmetry is broken by the nonlinear terms as soon as convection starts. However, the antisymmetric components can remain or become significant when it is fully developed [18–20].

In rotating double-diffusive convection the type of instability also depends on the combined direction of the compositional and temperature gradients. In spherical shells, with perfectly conducting boundaries and destabilizing compositional gradients, the patterns of convection are equatorially symmetric columnar ARWs. However, when the compositional gradient is stabilizing equatorially antisymmetric ARWs were also found for high compositional gradients [21]. The same Boussinesq approximation for a fluid sphere with internal compositional and heating sources or sinks, zero radial temperature and concentration fluxes at the boundary, and destabilizing compositional sources was studied in [19]. In this case, both types of convection were found without changing the compositional stratification.

The preferred eigenfunctions keep the invariance by rotation but break the equatorial symmetry, at the first bifurcation, for perfectly conducting fluid spheres with stress-free boundary conditions in the range of parameters found in [22–25]. The transition gives rise to axisymmetric latitudinal periodic oscillations (torsional oscillations, AP from now on), which are almost antisymmetric with respect to the equator. As for the ARWs, and at low Pr, the instability is due to the Coriolis force and consequently the angular frequency of the oscillations is $\mathcal{O}(\mathrm{Ek}^{-1})$ at onset. The boundaries of the region where these oscillations can arise from the conduction state were determined in [26]. At low Pr the AP oscillations consist of a poloidal vortex, which fills the sphere and reverses its rotation every half period, and an azimuthal motion with opposite velocities in each hemisphere, which also changes its direction but with a phase shift relative to the poloidal field. This velocity field gives rise to a latitudinal transport of the kinetic energy on the surface of the sphere in contrast to the ARWs. See Fig. 5 in [25] to visualize a typical periodic torsional flow.

It was recently found that, when the flattening of a stellar body due to the centrifugal force is very strong, the globally most common ARWs can switch to a zonal (axisymmetric) equatorially symmetric oscillation [27, 28]. Consequently, the literature shows that different formulations of the problem with the adequate set of parameters can give rise to patterns of inertial oscillations with any possible type of axial and equatorial symmetry in spherical and spheroidal geometry. Moreover, eigenfunctions with all possible symmetries are present in the leading spectra of the linear operators (eigenvalues of largest real part). Even when these eigenvalues are not unstable at the primary bifurcation, determining the pattern at the onset of the convection, they can give rise to stable large-scale flows by crossing forth and back the imaginary axis at a higher Ra than the critical [29, 30], or they can originate homoclinic or heteroclinic chains. That is, they can give rise to solutions whose trajectories evolve near a stable manifold, approaching a solution, and leaving their proximity by following an unstable direction. Then, they can approach again the same solution or another. Some examples of this kind of behavior were found in [20, 31]. Particularly striking is the dynamics described in [10] for Pr = 1, consisting of transitions from fully developed geostrophic turbulence, when the non-zonal energy is large, to axisymmetric convection about the rotation axis of the fluid sphere, when the zonal energy is orders of magnitude larger than the non-zonal.

The onset of convection in a differentially heated spherical shell with Robin boundary conditions for the temperature, $\partial_r \mathrm{T} + \mathrm{Bi}\,\mathrm{T} = 0$, and constant gravity, was studied in Ref. [11] for $\mathrm{Pr} = 0.03, 0.3, 3$ and 30, to simulate the former crystallization of a terrestrial magma ocean. It was found that the first instability is only affected by the Biot number, Bi, in the non-rotating case, and that the Robin condition can be replaced by a fixed flux when $\mathrm{Bi} \lesssim 0.03$ and by a fixed temperature when $\mathrm{Bi} \gtrsim 30$ [11]. That is, the ARWs continue to be the primary periodic flows at onset.

The present study is devoted to explore the influence of the Robin boundary conditions on the onset of convection in a fluid sphere, by determining the range of parameters where the torsional oscillations are preferred, following the methodology described in [26]. It shows that the existence of predominantly axisymmetric convective flows in rotating fluid spheres is independent of the boundary condition of the temperature. Moreover, it also shows than when Bi decreases the ratio $\mathrm{Pr}/\mathrm{Ek} = \mathcal{O}(10)$, found for $\mathrm{Bi} = \infty$, decreases following a law, which is fitted numerically. Similar laws are obtained for Ra_c, and the frequencies at onset. On the other hand, the manuscript describes in detail the physical meaning of taking a Robin boundary condition for the temperature, emphasizing the difference between the convective and radiative cases.

The remaining of the article is organized as follows: After the introduction, Sec. II is devoted to shortly introduce the mathematical model including the derivation of the temperature boundary conditions. Section IV shows the evolution of the marginal bicritical stability curves for several Bi, and Sec. V is the summary of the content.

II. FORMULATION OF THE PROBLEM

A fluid sphere rotating about the z-axis with constant angular velocity, $\boldsymbol{\Omega} = \Omega \hat{e}_z$, and uniformly internally heated is considered. A radial gravity $\mathbf{g} = -\gamma \boldsymbol{r}^*$, with $\gamma > 0$, corresponding to a uniform density, is assumed, $\boldsymbol{r}^*$ is the position vector, and the asterisc indicates from now on dimensional quantities. The Boussinesq approximation of the mass, momentum and energy equations is written in the rotating frame of reference of the sphere.

The centrifugal force is neglected since $\Omega^2/\gamma \ll 1$ in the major planets and most of the stars, and the density is also taken as constant in the Coriolis term. In addition, to write the equations in nondimensional form the radius of the sphere, r_o^*, is taken as scale for the distances, r_o^{*2}/ν for the time, and $\nu^2/\gamma\alpha r_o^{*4}$ for the temperature. The new physical constants in these expressions are the kinematic viscosity, ν, and the thermal expansion coefficient α.

The divergence-free nondimensional velocity field is written in terms of toroidal, Ψ, and poloidal, Φ, scalar potentials [32], i.e.,

$$\boldsymbol{v} = \boldsymbol{\nabla} \times (\Psi \boldsymbol{r}) + \boldsymbol{\nabla} \times \boldsymbol{\nabla} \times (\Phi \boldsymbol{r}).$$

The equations for Ψ and Φ are the radial components of the curl and double curl of the Navier-Stokes equations. Moreover, that for the energy is written in terms of the perturbation of the temperature, Θ, of the spherical symmetric conduction state ($\boldsymbol{v} = \boldsymbol{0}$, $\mathrm{T} = \mathrm{T}_c(r)$). The latter depends on the boundary conditions at the surface of the sphere. The spherical coordinates are (r, θ, φ), θ measuring the colatitude and φ the longitude. With the nondimensional full temperature written as $\mathrm{T}(t, r, \theta, \varphi) = \mathrm{T}_c(r) + \Theta(t, r, \theta, \varphi)$, the equations are

$$(\partial_t - \Delta)\, \mathcal{L}_2 \Psi = 2\mathrm{Ek}^{-1}\, (\partial_\varphi \Psi - \mathcal{Q}\Phi) - \boldsymbol{r} \cdot \boldsymbol{\nabla} \times (\boldsymbol{\omega} \times \boldsymbol{v}), \tag{1}$$

$$(\partial_t - \Delta)\, \mathcal{L}_2 \Delta\Phi = 2\mathrm{Ek}^{-1}\, (\partial_\varphi \Delta\Phi + \mathcal{Q}\Psi) - \mathcal{L}_2\Theta + \boldsymbol{r} \cdot \boldsymbol{\nabla} \times \boldsymbol{\nabla} \times (\boldsymbol{\omega} \times \boldsymbol{v}), \tag{2}$$

$$(\mathrm{Pr}\partial_t - \Delta)\, \Theta = \mathrm{Ra}\mathcal{L}_2\Phi - \mathrm{Pr}(\boldsymbol{v} \cdot \boldsymbol{\nabla}\Theta), \tag{3}$$

where $\boldsymbol{\omega} = \boldsymbol{\nabla} \times \boldsymbol{v}$ is the vorticity. The operators $\mathcal{L}_2$ and $\mathcal{Q}$ are defined as $\mathcal{L}_2 = -r^2\Delta + \partial_r(r^2\partial_r)$ and $\mathcal{Q} = r\cos\theta\Delta - (\mathcal{L}_2 + r\partial_r)(\cos\theta\partial_r - r^{-1}\sin\theta\partial_\theta)$. The symbol ∂_* means local derivative with respect to the corresponding subscript.

The non-dimensional parameters are the Rayleigh, Prandtl and Ekman numbers, defined as

$$\mathrm{Ra} = \frac{q\gamma\alpha r_o^{*6}}{3c_p\kappa^2\nu}, \qquad \mathrm{Pr} = \frac{\nu}{\kappa}, \quad \text{and} \qquad \mathrm{Ek} = \frac{\nu}{\Omega r_o^{*2}}, \tag{4}$$

respectively. The constant q accounts for the rate of internal heat generation per unit mass, c_p for the specific heat at constant pressure, and κ for the thermal diffusivity. With the present formulation the conduction state is always a solution for any value of the parameters, although unstable for large enough Ra.

Stress-free and impenetrable boundary conditions are used for the velocity field. In terms of the velocity potentials they mean

$$\Phi = \partial^2_{rr}\Phi = \partial_r(\Psi/r) = 0 \qquad \text{at} \qquad r = r_o. \tag{5}$$

The Robin boundary condition for the temperature is derived from a balance between the conductive heat flux density, $\mathbf{q} = -K_T \boldsymbol{\nabla}\mathrm{T}^*$, inside the sphere and the external convective or radiative heat flux [11], both normal to the external surface. In the first case, taking a constant temperature, T^*_a, outside the sphere of thermal conductivity K_T, and a convective heat transfer coefficient h, the balance leads to

$$\partial_{r^*}\mathrm{T}^*(r^*_o) = -\frac{h}{K_T}(\mathrm{T}^*(r^*_o) - \mathrm{T}^*_a). \tag{6}$$

Taking into account that $\mathrm{T}^* = \mathrm{T}^*_{\mathrm{c}} + \Theta^*$, where $\mathrm{T}^*_{\mathrm{c}}$ means the conductive temperature, solution of $\kappa\Delta\mathrm{T}^* = -q/c_p$, and that $\mathrm{T}^*_{\mathrm{c}}$ also fulfills Eq. (6), the Robin boundary condition for Θ^* becomes

$$\partial_{r^*}\Theta^*(r^*_o) + \frac{h}{K_T}\,\Theta^*(r^*_o) = 0 \tag{7}$$

independent of T^*_a. In nondimensional form it becomes

$$\partial_r\Theta + \mathrm{Bi}\,\Theta = 0 \qquad \text{at} \qquad r = r_o, \tag{8}$$

the Biot number being

$$\mathrm{Bi} = \frac{hr^*_o}{K_T}. \tag{9}$$

It is defined analogously to the Biot number used for solid surfaces in contact with a fluid. It introduces a measure of the external resistance to the heat transport through the coefficient h.

With the boundary condition (6) the nondimensional conductive temperature is

$$\mathrm{T}_{\mathrm{c}}(r) = \frac{1}{2}\mathrm{Ra}\,\mathrm{Pr}^{-1}(1 - r^2) + \mathrm{T}_{\mathrm{c}}(r_o), \tag{10}$$

and $\mathrm{T}_{\mathrm{c}}(r_o) = \mathrm{Ra}\,\mathrm{Pr}^{-1}\,\mathrm{Bi}^{-1} + \mathrm{T}_a$.

A second possibility is to consider a radiative heat balance as in [11]. This leads to a nonlinear boundary condition because the Stefan-Boltzmann law governs the heat transport in the exterior of the sphere, then

$$\partial_{r^*}\mathrm{T}^*(r^*_o) = -\frac{\beta\sigma}{K_T}(\mathrm{T}^{*4}(r^*_o) - \mathrm{T}^{*4}_a), \tag{11}$$

where σ is the Stefan-Boltzmann constant, and β the emissivity coefficient, which is $\beta = 1$ for the black-body radiation.

To obtain the boundary condition for Θ^*, to analyze the stability of the conduction state, Eq. (11), with $\mathrm{T}^* = \mathrm{T}^*_c + \Theta^*$, is first linearized about T^*_c. Then, taking into account that T^*_c fulfills Eq. (11),

$$\partial_{r^*}\Theta^*(r^*_o) + \frac{4\sigma \mathrm{T}^{*3}_{\mathrm{c}}(r^*_o)}{K_T}\,\Theta^*(r^*_o) = 0. \tag{12}$$

In nondimensional form it can be written as Eq. (8) with the radiative Biot number

$$\mathrm{Bi}_r = \frac{4r^*_o\sigma \mathrm{T}^{*3}_{\mathrm{c}}(r^*_o)}{K_T}. \tag{13}$$

By analogy with the previous case, a radiative heat transfer coefficient $h_{\mathrm{r}} = 4\sigma \mathrm{T}^{*3}_{\mathrm{c}}(r^*_o)$ can be defined. The linearized boundary condition gives formally the same expression as the nondimensional conductive temperature (10), but now $\mathrm{T}_{\mathrm{c}}(r_o)$ must be determined by solving the equation $\mathrm{T}^4_{\mathrm{c}} - 4\mathrm{T}^3_{\mathrm{c}}\,\mathrm{Bi}_r^{-1}\,\mathrm{Ra}\,\mathrm{Pr}^{-1} - \mathrm{T}^4_a = 0$ at $r = r_o$, to obtain the value of the full temperature. This means that at the onset of convection the change from convective to radiative boundary conditions only modifies the full temperature profile; however, it must be taken into account that in order to solve the stability problem the Stefan-Boltzmann law is linearized. In the nonlinear problem the full fourth degree condition should be applied, and the velocity and vorticity fields would also be different in the two cases.

In any case regularity conditions are always enforced at $r = 0$.

Equations (1)-(3) with boundary conditions (5) and (8) are $\mathcal{SO}(2) \times \mathcal{Z}_2$-equivariant, $\mathcal{SO}(2)$ generated by azimuthal rotations of an arbitrary angle φ_0, and $\mathcal{Z}_2$ by reflections with respect to the equatorial plane, i.e., the actions

$$\mathcal{R}_{\varphi_0}: \qquad (\Psi,\Phi,\Theta)(t,r,\theta,\varphi) \to (\Psi,\Phi,\Theta)(t,r,\theta,\varphi+\varphi_0), \tag{14}$$

$$\zeta_\theta: \qquad (\Psi,\Phi,\Theta)(t,r,\theta,\varphi) \to (-\Psi,\Phi,\Theta)(t,r,\pi-\theta,\varphi), \tag{15}$$

leave the system invariant.

III. NUMERICAL METHODS

We are interested in the stability of the conduction state, which in terms of the potentials and Θ is $(\Psi_c,\Phi_c,\Theta_c) = (0,0,0)$. Then, since the nonlinear terms of Eqs. (1)-(3) are quadratic, their linearization at the conduction state is

$$
\begin{aligned}
(\partial_t - \Delta)\mathcal{L}_2\Psi &= 2\mathrm{Ek}^{-1}\,(\partial_\varphi\Psi - \mathcal{Q}\Phi), && (16)\\
(\partial_t - \Delta)\mathcal{L}_2\Delta\Phi &= 2\mathrm{Ek}^{-1}\,(\partial_\varphi\Delta\Phi + \mathcal{Q}\Psi) - \mathcal{L}_2\Theta, && (17)\\
(\mathrm{Pr}\,\partial_t - \Delta)\,\Theta &= \mathrm{Ra}\,\mathcal{L}_2\Phi, && (18)
\end{aligned}
$$

with boundary conditions (5) and (8). The functions (Ψ, Φ, Θ) are first expanded in spherical harmonic series with a triangular truncation of maximal degree L,

$$
(\Psi, \Phi, \Theta)(t, r, \theta, \varphi) = \sum_{l=0}^{L} \sum_{m=-l}^{l} (\Psi_l^m, \Phi_l^m, \Theta_l^m)(r, t) Y_l^m(\theta, \varphi), \tag{19}
$$

with $\Psi_l^{-m} = \overline{\Psi_l^m}$, $\Phi_l^{-m} = \overline{\Phi_l^m}$, $\Theta_l^{-m} = \overline{\Theta_l^m}$, and imposing $\Psi_0^0 = \Phi_0^0 = 0$ to uniquely determine the two scalar potentials. The spherical harmonics are normalized as

$$
Y_l^m(\theta, \varphi) = \sqrt{\frac{2l+1}{2}\frac{(l-m)!}{(l+m)!}} P_l^m(\cos\theta) e^{im\varphi} \quad l \geq 0, \quad 0 \leq m \leq l,
$$

P_l^m being the associated Legendre functions of degree l and order m. Then the eigenvalue problem separates into one for each azimuthal wave number m of the form

$$
\begin{aligned}
\lambda\Psi_l^m &= \mathcal{D}_l\Psi_l^m + \frac{2\mathrm{Ek}^{-1}}{l(l+1)}\left(im\Psi_l^m - [\mathcal{Q}\Phi]_l^m\right), && (20)\\
\lambda\mathcal{D}_l\Phi_l^m &= \mathcal{D}_l^2\Phi_l^m - \Theta_l^m + \frac{2\mathrm{Ek}^{-1}}{l(l+1)}\left(im\mathcal{D}_l\Phi_l^m + [\mathcal{Q}\Psi]_l^m\right), && (21)\\
\lambda\Theta_l^m &= \mathrm{Pr}^{-1}\mathcal{D}_l\Theta_l^m + \mathrm{Pr}^{-1}l(l+1)\mathrm{Ra}\,\Phi_l^m, && (22)
\end{aligned}
$$

for $m \leq l \leq L$, $\mathcal{D}_l$ being the radial operator $\mathcal{D}_l = \partial_{rr}^2 + (2/r)\partial_r - l(l+1)/r^2$. The functions $(\Psi_l^m, \Phi_l^m, \Theta_l^m)$ depend now only on the radius. The boundary conditions decouple for each l and m, i.e.

$$
\partial_r(\Psi_l^m/r) = 0, \quad \Phi_l^m = 0, \quad \partial_{rr}^2\Phi_l^m = 0, \quad \text{and} \quad \partial_r\Theta_l^m + \mathrm{Bi}\Theta_l^m = 0 \tag{23}
$$

at $r = r_o$. The square bracket $[\cdot]_l^m$ indicates extracting the spherical harmonic coefficient of degree l and order m. The operator $\mathcal{Q}$ is

$$
[\mathcal{Q}f]_l^m = -(l-1)(l+1)c_l^m D_{1-l}^+ f_{l-1}^m - l(l+2)c_{l+1}^m D_{l+2}^+ f_{l+1}^m, \tag{24}
$$

$$
\text{with} \quad D_l^+ = \partial_r + \frac{l}{r}, \quad \text{and} \quad c_l^m = \left(\frac{l^2 - m^2}{4l^2 - 1}\right)^{1/2}. \tag{25}
$$

The final step in the discretization is applying a collocation method in the radial coordinate. A mesh of $N+1$ Gauss-Lobatto points is employed and the boundary conditions are included in the derivative matrices that substitute the operators $\mathcal{D}_l$, $\mathcal{D}_l^2$, and D_l^+ in the eigenvalue problem. Since the operator $\mathcal{Q}$ couples the coefficients of degrees $l-1$, l and $l+1$, the resulting matrix of the discretized problem has a block-tridiagonal structure. The operator $\mathcal{D}_l$ in the left hand side of Eq. (21) is invertible, and then the eigenvalue problem (20)-(22), for a given azimuthal wave number m, can be written as a standard one

$$\mathcal{A}_m(\mathrm{Ra}, \mathrm{Ek}, \mathrm{Pr}, \mathrm{Bi})X_m = \lambda X_m, \tag{26}$$

$X_m = (\Psi_m, \Phi_m, \Theta_m)$ being now a vector of dimension $3(L-m+1)(N-1)$ if $m \neq 0$ and $3L(N-1)$ if $m=0$, containing the values of the amplitudes of the potentials and the perturbation of the temperature in spherical harmonics at the $N-1$ inner collocation points.

When the transition curves presented depend on just one parameter, the rest are fixed except Ra. Its critical value, Ra_c, corresponds to the condition $\Re(\lambda) = 0$. The leading spectra (a set of eigenvalues of maximal real part) of $\mathcal{A}_m$ are computed by using a complex shift-invert strategy (see Refs. [22, 33] for details). The critical curves can also be found by applying continuations methods to the eigenvalue problem. This is always done to track the curves of double-Hopf points at which there is a simultaneous bifurcation to two different azimuthal wave numbers m_1 and m_2 (see Sect. 3 of Ref. [26]).

IV. DESCRIPTION OF THE RESULTS

A. Marginal stability curves versus Bi

Figure 1 shows the dependence of Ra_c versus Bi for sets of parameters for which the torsional solutions obtained by taking the condition $\Theta(r_o) = 0$ ($\mathrm{Bi} \to \infty$) are preferred. It illustrates very well the two limit cases discussed in Sec. II, and the transition zone for $10^{-2} \lesssim \mathrm{Bi} \lesssim 10^2$. When Bi decreases the thermal flux through the boundary drops, and Ra_c starts to decrease due to the raise of the heat stored in the fluid mass. At very low Pr [Fig. 1(a)] the latitudinal oscillations of angular frequency $\omega = 2 \times 10^6$ existing at large Bi are superseded by prograde ARWs of azimuthal wave number $m = 1$ ($m = 1p$) and $\omega = 3.95 \times 10^5$ due to the Robin boundary condition. Both ω remain almost constant along the curves. When Pr is increased [Figs. 1(b)-(c)] the change takes place at larger Bi. For

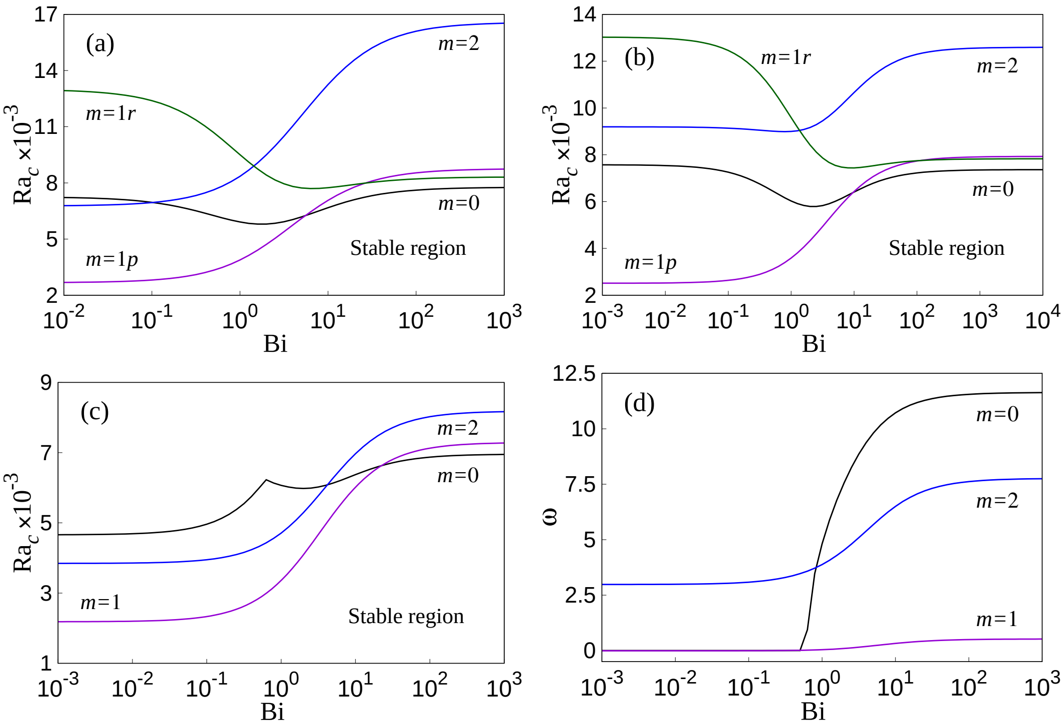

FIG. 1. Critical Rayleigh number, Ra_c, versus the Biot number, Bi, for (a) $\mathrm{Ek} = 4.47 \times 10^{-7}$ and $\mathrm{Pr} = 4 \times 10^{-6}$, (b) $\mathrm{Ek} = 10^{-3}$ and $\mathrm{Pr} = 0.01$, and (c) $\mathrm{Ek} = 2.12 \times 10^{-3}$ and $\mathrm{Pr} = 0.71$. The curves correspond to azimuthal wave numbers $m = 0$ (black), $m = 1$ with $\omega < 0$ ($m = 1p$, violet), $m = 1$ with $\omega > 0$ ($m = 1r$, green), and $m = 2$ (blue). (d) Frequency, ω, versus Bi for the parameters of (c).

instance, it occurs at $\mathrm{Bi} = 9.63$ for liquid sodium of $\mathrm{Pr} = 0.01$ [Fig. 1(b)]. At this point the oscillations of frequency $\omega = 888.06$ are replaced by prograde azimuthal waves of frequency $\omega = 171.96$ in the asymptotic limit $\mathrm{Bi} \to 0$. At the moderate $\mathrm{Pr} = 0.71$ of the hydrogen the frequency jumps at $\mathrm{Bi} = 22.33$ from latitudinal oscillations of $\omega = 11.64$ at $\mathrm{Bi} \to \infty$ to nearly stationary prograde waves of $\omega = 0.01$ at $\mathrm{Bi} \to 0$, before the axisymmetric mode becomes stationary. For this Pr the marginal frequency of the $m = 1$ mode changes sign at $\mathrm{Bi} \approx 0.247$, and there is a continuous transition from prograde to retrograde ($m = 1r$) marginal ARWs.

The contour plots of Θ maintain the shape of those with $\mathrm{Bi} = \infty$, but they expand towards the polar surface of the sphere when Bi decreases (see next section).

B. Marginal bicritical curves

In this section the techniques used in Ref. [26] for Bi $= \infty$ are used to show the dependence with Bi of the region of the parameter space inside which the first bifurcation is to axisymmetric torsional solutions. The critical curves for the transitions to $m = 0$ and $m = 1$ versus Pr were first computed for a fixed value of the Ekman number Ek $= 10^{-3}$, and for several values of Bi (10^{-4}, 10^{-2}, 10^{-1}, 1, 2, 5, 10, 10^2 and ∞). Figure 2 shows four cases, the rest are similar and therefore are not shown. As seen before, there are in general two curves of $m = 1$ corresponding to prograde and retrograde traveling waves, respectively. The interval in which the first transition is to axisymmetric solutions is bounded by two double-Hopf points, the left for $m = 0$ and $m = 1r$, and the right for $m = 0$ and $m = 1p$. As Bi increases the interval moves to the right in the Pr axis, and the critical Rayleigh number also increases. To compute the full region where the torsional mode is preferred, the curves of double-Hopf points were tracked for every of the Bi already mentioned.

The extended system to follow the simultaneous bifurcation to wave numbers $m = m_1$ and $m = m_2$ is

$$(\mathcal{A}_{m_1}(\mathrm{Ra}, \mathrm{Ek}, \mathrm{Pr}, \mathrm{Bi}) - i\omega_{m_1}\mathcal{I})\, X_{m_1} = 0, \tag{27}$$

$$(\mathcal{A}_{m_2}(\mathrm{Ra}, \mathrm{Ek}, \mathrm{Pr}, \mathrm{Bi}) - i\omega_{m_2}\mathcal{I})\, X_{m_2} = 0, \tag{28}$$

$$\|X_{m_1}\|^2 = 1, \tag{29}$$

$$\langle \Re(X_{m_1}), \Im(X_{m_1}) \rangle = 0, \tag{30}$$

$$\|X_{m_2}\|^2 = 1, \tag{31}$$

$$\langle \Re(X_{m_2}), \Im(X_{m_2}) \rangle = 0. \tag{32}$$

The first two equations establish that there are two simultaneous Hopf bifurcations to wave numbers m_1 and m_2 (0 and 1 in our case), with frequencies ω_{m_1} and ω_{m_2}, and eigenvectors X_{m_1} and X_{m_2}. The last four equations are normalizing conditions for the complex eigenvectors. Two of them fix their norm and the other two their phases. If the dimensions of $\mathcal{A}_{m_1}$ and $\mathcal{A}_{m_2}$ are n_1 and n_2, respectively, there are $2n_1 + 2n_2 + 4$ real equations, and $2n_1 + 2n_2 + 5$ unknowns $(X_{m_1}, X_{m_2}, \omega_{m_1}, \omega_{m_2}, \mathrm{Ra}, \mathrm{Ek}, \mathrm{Pr})$ because Bi is kept fixed. Therefore the other three nondimensional parameters are obtained during the continuation. It turns out that the two double-Hopf points on the $m = 0$ curve in each of the plots of Fig. 2 are on the same bicritical curve, because it has a turning point as can be seen in Fig. 3(a). It

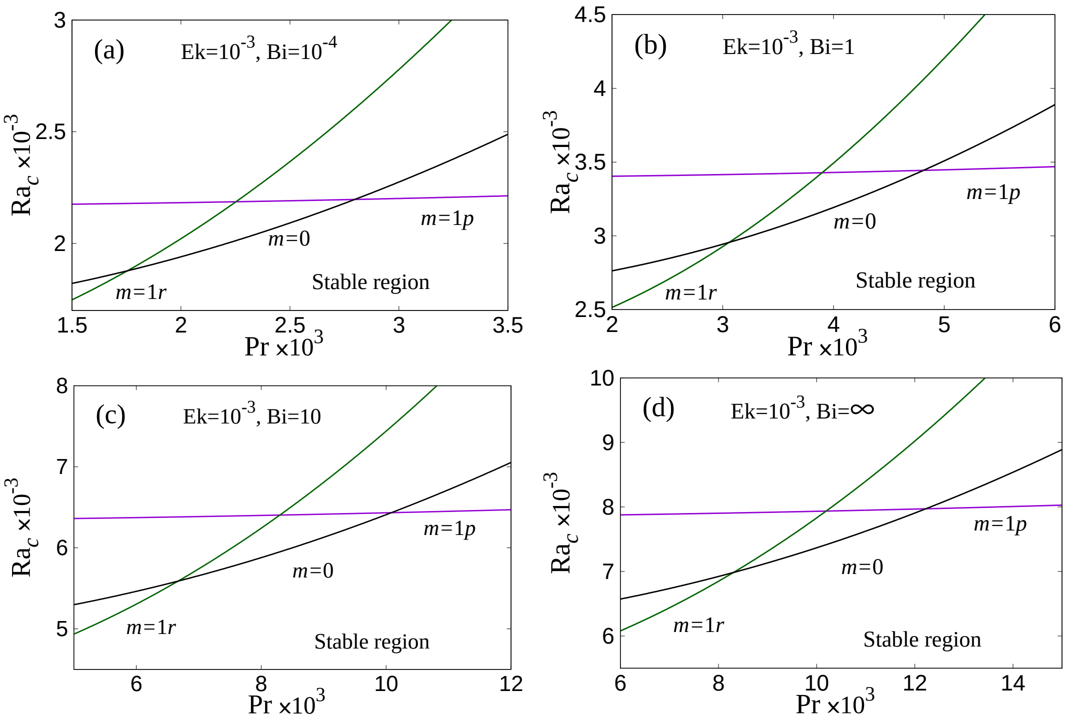

FIG. 2. Transition curves from the conduction state for $\mathrm{Ek} = 10^{-3}$ and Biot numbers (a) 10^{-4}, (b) 1, (c) 10, and (d) ∞. The intersections of the curves provide the initial conditions for the double-Hopf continuation. The label and color conventions are the same as in Fig. 1. The conduction state is unstable above the lower envelope of the three curves, and the flow is axisymmetric inside the curvilinear triangle bounded by the three curves.

shows the regions inside which the first bifurcation is to $m = 0$. If Pr and Ek are taken inside one of these regions, Bi is kept fixed to the value of the corresponding region, and Ra is increased from a low value, then the first transition is to an axisymmetric periodic solution, i.e., a torsional flow. The dot in each curve indicates the change of sign of the frequency ω_1 for the wave number $m = 1$. Along the direct segment between the origin and the dot the frequency is negative (prograde waves). Along the rest its is positive (retrograde waves). The dots are concentrated close to $\mathrm{Ek} = 4.4 \times 10^{-2}$. The curves for $\mathrm{Bi} = 10^2$ and $\mathrm{Bi} = \infty$ are cut by segments of the multicritical curves of $m = 0$ and $m = 2$, near Pr=0.9 [it can also be seen in Fig. 4(a)]. This does not hold for the rest of Bi considered. Sect. 4 of Ref. [26] explains how the double-Hopf curves are explored to find other bifurcations that occur along them. This is what happens in the two mentioned cases, adding a new segment

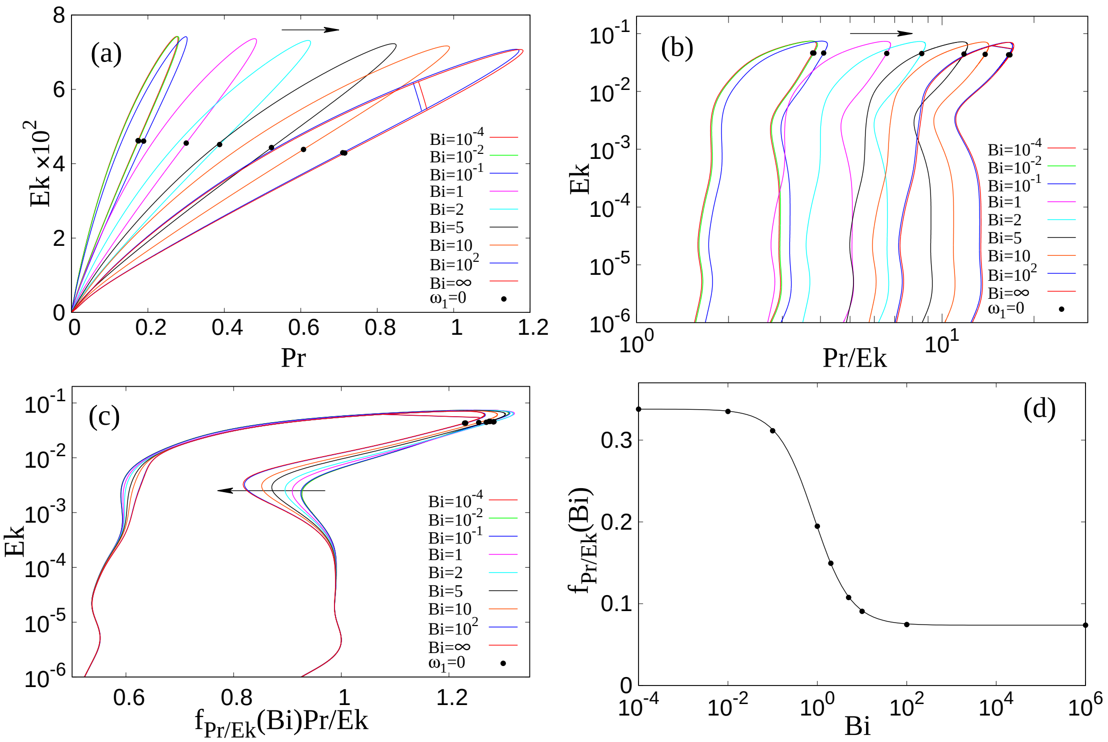

FIG. 3. (a) Curves of double-Hopf bifurcations for the values of Bi indicated in the legend. (b) The same curves in logarithmic scale, and with Pr/Ek in the horizontal axis. (c) Same as (b) but with the scaling of Pr/Ek shown in (d). In all plots the arrow indicates the direction of increasing Bi. The dots in plots (a) to (c) indicate the change of sign of the frequency ω_1.

of a curve limiting the upper part of the region (higher Pr). It can be seen that the region shrinks when Bi decreases. Those for $\mathrm{Bi} = 10^{-4}$ and $\mathrm{Bi} = 10^{-2}$ can hardly be distinguished, indicating that there is a non-empty limit region when $\mathrm{Bi} \to 0$.

The shape of the curves looks very similar when the horizontal axis is scaled with Ek and they are represented in logarithmic scale. In addition, this scale blows up the limit $\mathrm{Ek} \to 0$ [see Fig. 3(b)]. There is a multiplicative factor $\mathrm{f}_{\mathrm{Pr/Ek}}(\mathrm{Bi})$ that makes them to almost overlap [see Fig. 3(c)]. The factor was found in order to move the maxima of Pr/Ek for low Ek to $\mathrm{f}_{\mathrm{Pr/Ek}}(\mathrm{Bi})\mathrm{Pr/Ek} = 1$, and it is shown in Fig. 3(d). The dots are the computed values, and the curve is the best fit to a function of the form

$$\mathrm{f}(\mathrm{Bi}) = \mathrm{f}(\infty) + \left(\mathrm{f}(0) - \mathrm{f}(\infty)\right)/(1 + c\,\mathrm{Bi}^{p}), \tag{33}$$

using the nonlinear least-squares Marquardt-Levenberg algorithm, implemented in Gnuplot [34]. The value $\mathrm{f}(\mathrm{Bi} = 0)$ was taken as that at $\mathrm{Bi} = 10^{-4}$, and $\mathrm{Bi} = \infty$ was substituted,

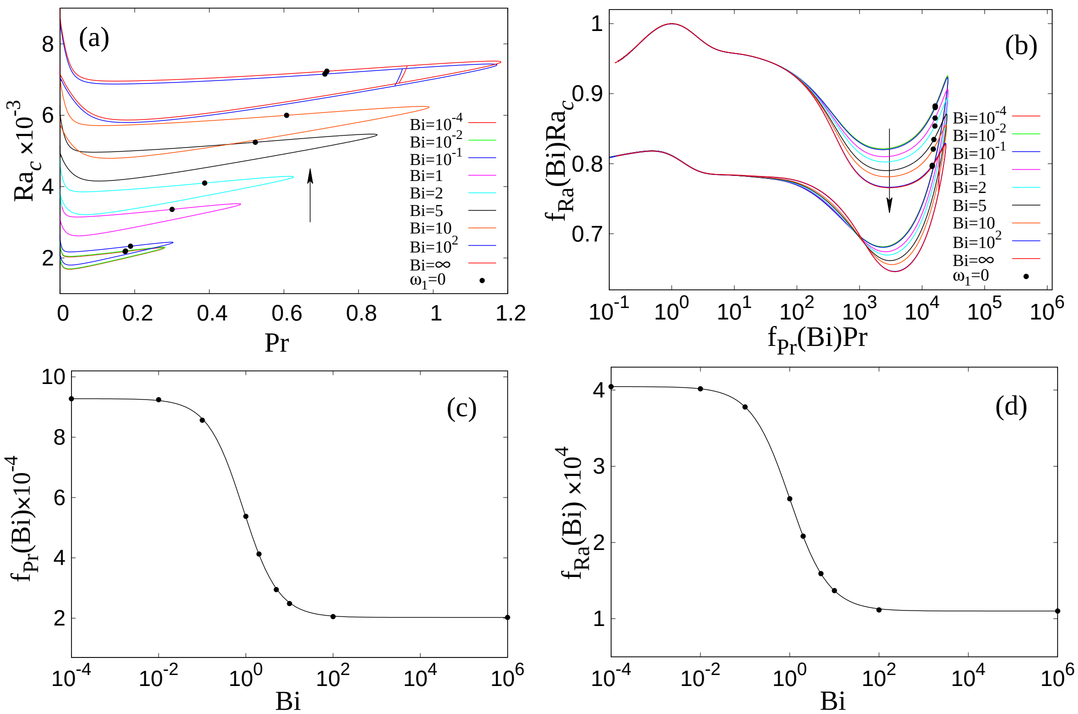

FIG. 4. (a) Critical Ra along the curves of double-Hopf bifurcations of Fig. 3(a). (b) Same as (a) but in log–linear scale, and with the scalings of Pr and Ra_c shown in (c) and (d). In all plots the arrow indicates increasing Bi, which is indicated in the legends. The dots in plots (a) and (b) indicate the same as in Fig. 3.

in this and all similar subsequent plots, by $Bi = 10^6$. In this case the fitting gives $c = 1.200$ and $p = 1.0587$. This plot confirms that all the substantial changes take place, approximately, in the interval $10^{-2} \lesssim Bi \lesssim 10^2$. Figure 3(c) indicates some kind of universal behavior for low Ek, when Pr/Ek is appropriately scaled by a function of Bi. The same holds with the critical Ra along the double-Hopf curves as can be seen in Fig. 4. For low Pr (which also means low Ek) the curves overlap when both parameters (Pr and Ra) are scaled as shown in Figs. 4(c) and (d). The fitting parameters are now $c = 1.1813$ and $p = 1.0693$, and $c = 0.9992$ and $p = 1.0018$, respectively. Fig. 4(a) shows how Ra_c decreases when $Bi \to 0$, because in this limit the wall becomes insulating and the heat accumulated in the fluid makes the conduction state more unstable.

Figures 5(a) and (c) show the absolute value of the frequencies ω_0 and ω_1 for the transitions to solutions with azimuthal wave numbers $m = 0$ and $= 1$, respectively, along the curves of double-Hopf points. In the case of ω_0 the eigenvalue problem is real, and there

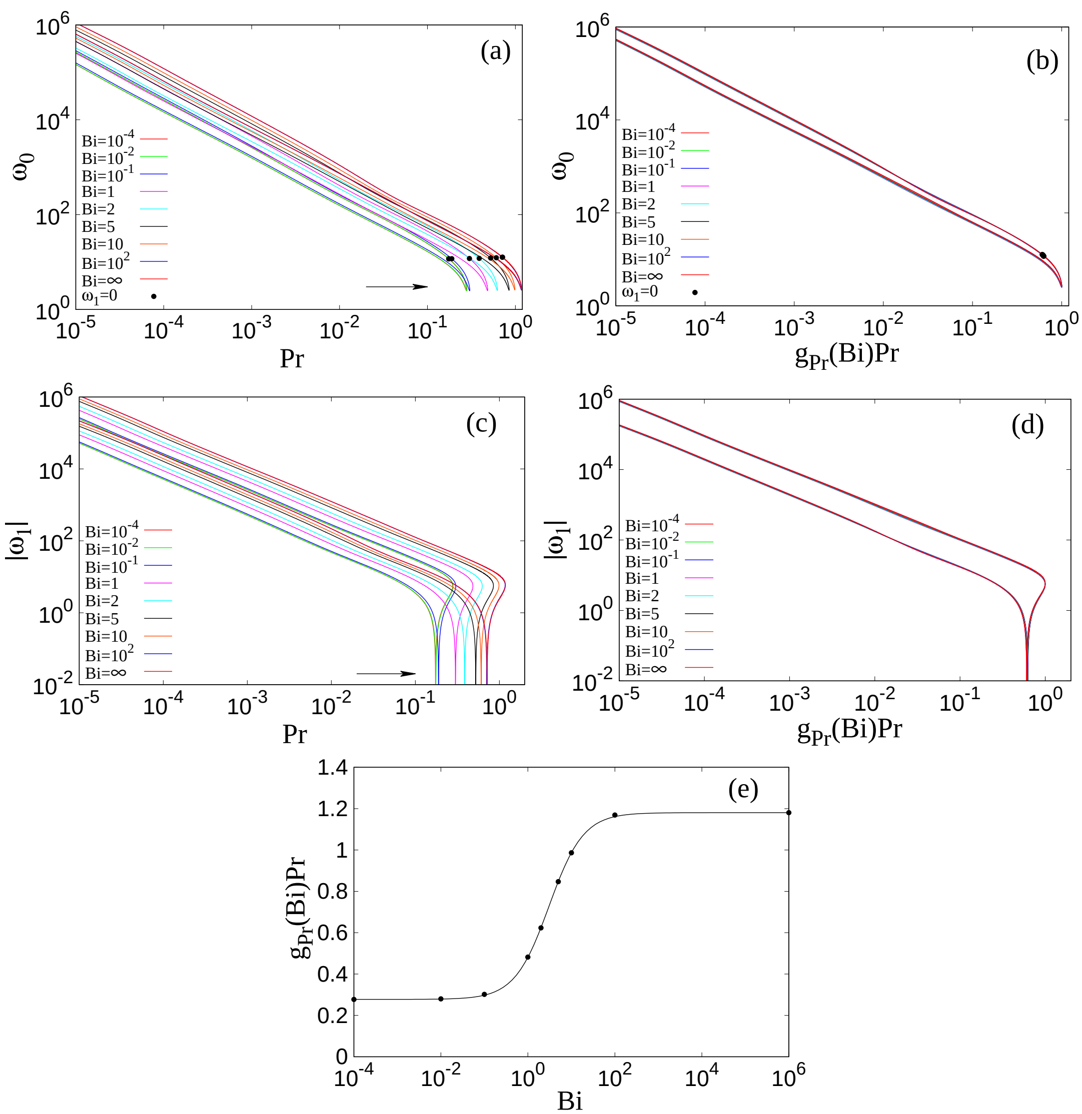

FIG. 5. Critical frequencies (a) ω_0, and (c) ω_1 along the curves of double-Hopf bifurcations in Fig. 3(a). (b) and (d) same as (a) and (c) but with the same scaling, $g_{\mathrm{Pr}}(\mathrm{Bi})$, of Pr shown in (e).

is a complex pair $\pm i\omega_0$ at the bifurcation whose positive imaginary part is shown. It never reaches zero. In the case of $m = 1$ the eigenvalue problem is complex and the sign of ω_1 determines, as seen before, if the waves are prograde or retrograde. The changes of sign, indicated in the previous figures with dots, are seen now as vertical peaks in logarithmic scale. The upper part of the curves correspond to retrograde ARWs, and the lower to prograde.

As in the previous two figures, by scaling Pr it is possible to overlap the curves, as can be seen in Figs. 5(b) and (d). The common multiplicative factor $g_{\mathrm{Pr}}(\mathrm{Bi})$ is shown in Fig. 5(e).

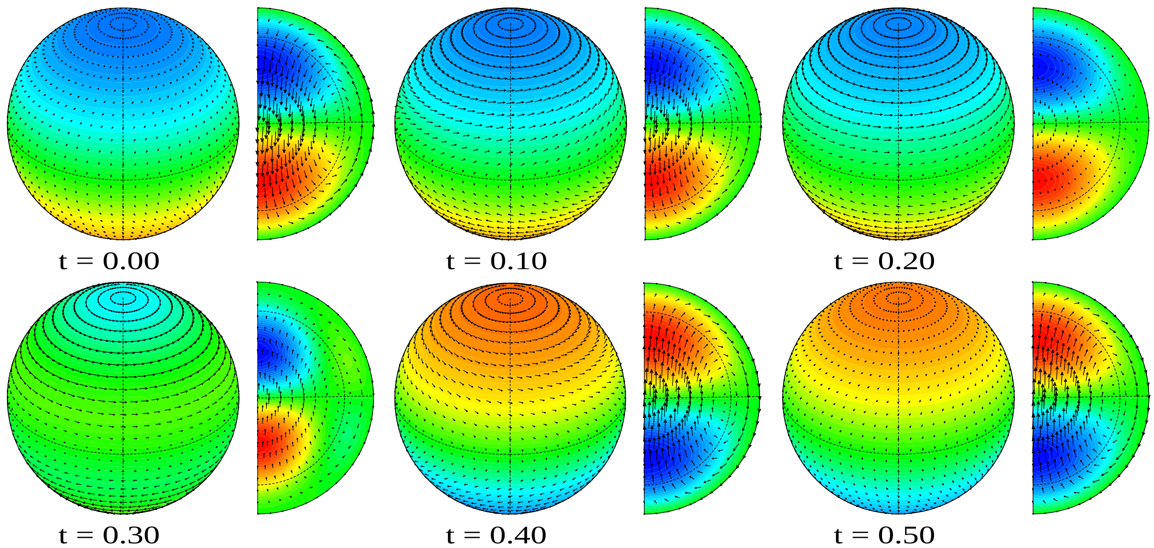

FIG. 6. Time evolution of the contour plots of Θ and velocity field of the torsional mode ($m = 0$) for $\mathrm{Bi} = \infty$, $\mathrm{Pr} = 1.22 \times 10^{-2}$, $\mathrm{Ek} = 10^{-3}$, and $\mathrm{Ra} = 7969$.

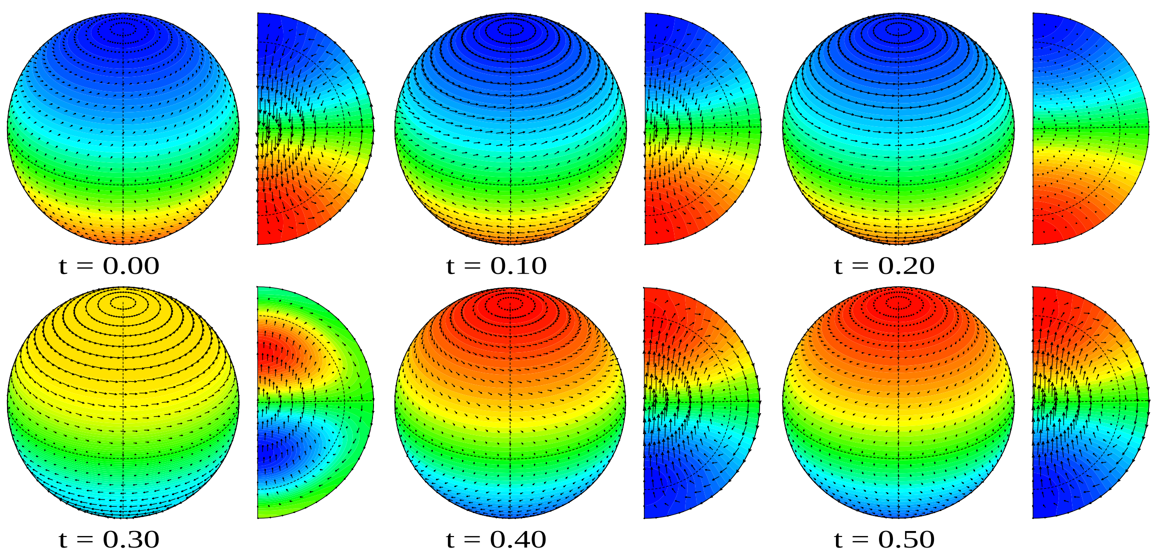

FIG. 7. Same as Fig. 6 for $\mathrm{Bi} = 10^{-4}$, $\mathrm{Pr} = 2.80 \times 10^{-3}$, $\mathrm{Ek} = 10^{-3}$, and $\mathrm{Ra} = 2198$.

It has been selected to overlap the turning points of all curves to $\mathrm{g_{Pr}(Bi)Pr} = 1$. The fitting parameters to a function also of the form (33) are $c = 0.2999$ and $p = 1.1007$.

Inside the region of preferred $m = 0$ solutions, the ratio Pr/Ek is close to constant [see Figs. 3(b) and (c)], and therefore if Pr is substituted in Fig. 5 by Ek the plots are very similar. A power law fitting to the curves in the low Ek limit shows that $\omega = \mathcal{O}(\mathrm{Ek}^{-1})$,

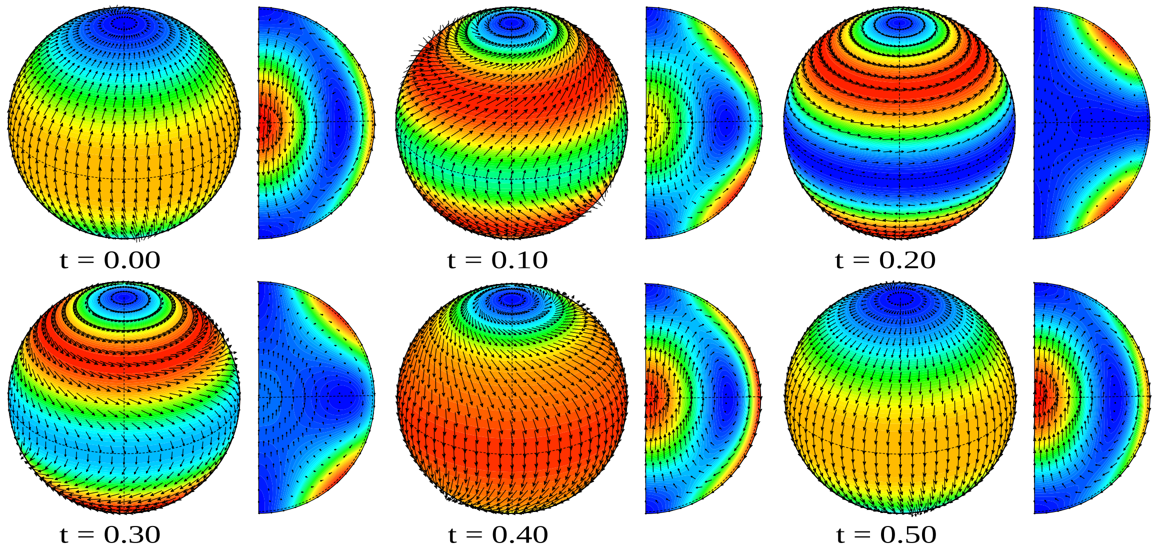

FIG. 8. Same as Fig. 6 but for the kinetic energy density. The superposed velocity field is the same.

indicating that both modes are inertial; namely, that the Coriolis force is responsible for the instability.

The results shown in Figs. 2 and 3 help to understand what happens in the plots of Fig. 1. If only Bi is decreased from a high value it is not possible to have $m = 0$ as the first bifurcation in all its range of variation. As mentioned before, the interval of Pr for which the first bifurcation is to $m = 0$ moves to smaller values as Bi decreases. For instance, the intervals of preferred wave number $m = 0$ for Bi = 1 and Bi = 10, and a common Ek = 10^{-3}, are disjoint (see Fig. 2). Figure 3(b) shows that, if Bi is fixed, the ratio Pr/Ek must be kept almost constant to always be inside the $m = 0$ region. The value Pr/Ek = $\mathcal{O}(10)$ was already given in Ref. [22] and confirmed by the asymptotic calculation in Ref. [23] when Bi = ∞. Figure 3(c) shows that if Bi is moved the parameter that must be kept fixed to be in the $m = 0$ region is $\mathrm{f}_{\mathrm{Pr/Ek}}(\mathrm{Bi})\mathrm{Pr/Ek}$.

Figures 6 and 7 show the time evolution of the contour plots of Θ and the velocity field of a torsional mode for Bi = ∞ and Bi = 10^{-4}. The rest of the parameters correspond to those at the intersection of the transition curves to $m = 0$ and $m = 1p$ of Figs. 2(d) and (a), respectively. They are specified in the caption of the figures. The spherical section taken is indicated in the meridional section with a dashed circle, which is very close to the surface for the kinetic energy density, K (Fig. 8). The time shown is the fraction of the period of

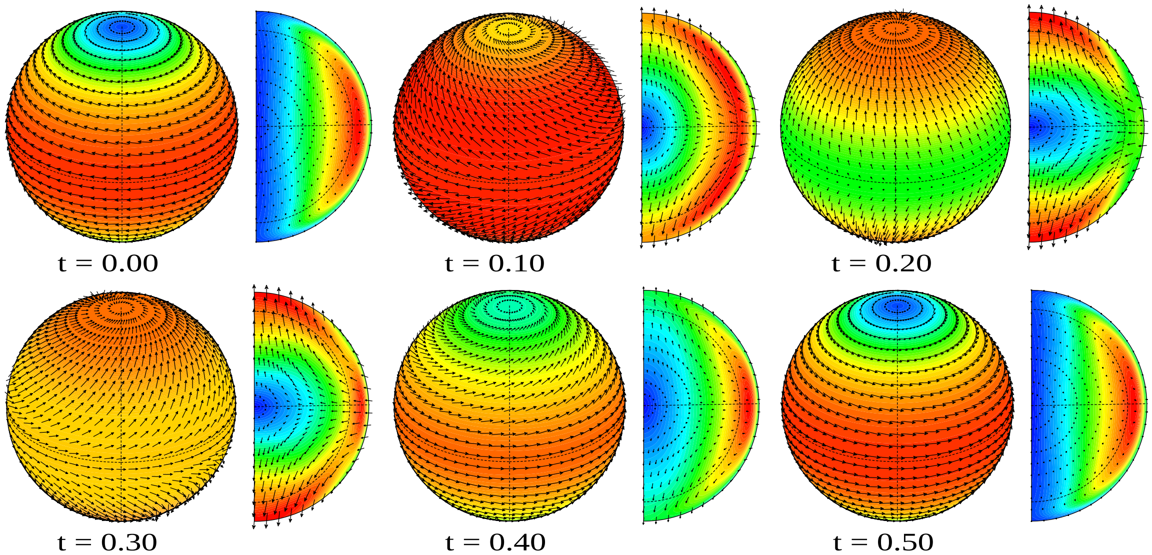

FIG. 9. Same as Fig. 6 but for the Euclidean norm of the vorticity and the vorticity field.

the eigenfunction. Only half the period is shown since the rest can be obtained by applying the spatio-temporal symmetries of the torsional solutions. They are symmetric cycles, which satisfy, in terms of the velocity field, $(v_r, v_\theta, v_\varphi)$, and Θ

$$(v_r, v_\theta, v_\varphi)(t, r, \theta, \varphi) = (v_r, v_\theta, v_\varphi)(t, r, \theta, \varphi + \varphi_0), \tag{34}$$

$$(v_r, v_\theta, v_\varphi)(t + T/2, r, \theta, \varphi) = (v_r, -v_\theta, v_\varphi)(t, r, \pi - \theta, \varphi). \tag{35}$$

$$\Theta(t, r, \theta, \varphi) = \Theta(t, r, \theta, \varphi + \varphi_0), \tag{36}$$

$$\Theta(t + T/2, r, \theta, \varphi) = \Theta(t, r, \pi - \theta, \varphi). \tag{37}$$

The main difference between both cases is that for Bi $= \infty$ the boundary condition for the temperature is $\Theta = 0$, preventing the perturbation from reaching $r = r_o$, while for small Bi (10^{-4} in Fig. 7) it does. The structure of the velocity field does not change, and therefore neither that of the vorticity. Figure 8 displays K for Bi $= \infty$, and the same parameters as in Fig. 6. It concentrates at mid latitudes close to the surface of the sphere, when the longitudinal velocity is at a maximum, and close to the center, when the meridional velocity is at a maximum. The corresponding plots for Bi $= 10^{-4}$ are not presented because they look alike. The velocity field of these plots shows the dynamics of the torsional solutions. They can be seen as the superposition of a single meridional vortex that changes the sense of rotation each half period, and a zonal (azimuthal) wind that goes to the east in one hemisphere and to the west in the other, changing the direction also every half period but with a phase shift of a quarter of period (see Figs. 6 and 7). This can also be seen in Fig. 9. It shows the contour plots of the norm of the vorticity, and the vorticity field, for the same parameters as in Fig. 6 . At $t = 0.00$ the velocity is mainly meridional, its azimuthal component is very small and, consequently, the largest component of the vorticity is longitudinal. At $t = 0.20$ the meridional velocity is very small and the azimuthal component is maximal at high latitudes, where the vorticity has a strong component along the axis of rotation, with opposite directions in each hemisphere. At the equator and close to the surface of the sphere, where the azimuthal component of the velocity changes sign, the equatorial component of the vorticity becomes large, signaling an increased shear.

Figure 10 shows the eigenfunctions corresponding to the azimuthal wave number $m = 1$ at the same double-Hopf points as in Figs. 6 and 7. The equatorial section has been included in this case, and the meridional section taken is indicated in the equatorial section with a dashed line. The first row for $\mathrm{Bi} = \infty$ and the fourth for $\mathrm{Bi} = 10^{-4}$ display the same difference as in the $m = 0$ case. The perturbation of the temperature reaches the boundary in the second case but not in the first for the same reason as before. Both transitions to $m = 0$ and to $m = 1$ occur at lower Ra when Bi goes to zero, but the critical Ra for those of $m = 1$ decreases a little faster. This explains why the region for the onset of the torsional solutions becomes smaller as Bi decreases. This effect could already be seen in the plots of Fig. 2. The contour plots of K and the vorticity are only shown for $\mathrm{Bi} = \infty$ in Fig. 10 because they are very similar when $\mathrm{Bi} = 10^{-4}$. The solutions are ARWs and the time evolution is just a rigid rotation of the scalar and vector fields in the figure, with the maxima of K at the surface of the sphere, and the vorticity mainly aligned with the axis of rotation as happens for the Taylor columns.

V. SUMMARY AND CLOSING REMARKS

The linear stability analysis of the conduction state and the continuation of bicritical points in a fluid sphere with Robin boundary conditions for the temperature field show that:

- The change from perfectly conducting to Robin boundary conditions produces a significant decrease of Ra_c in the range $10^{-2} \lesssim \mathrm{Bi} \lesssim 10^2$, and an expansion of the torsional oscillations to the boundary of the sphere, due to the fall of the heat released to the

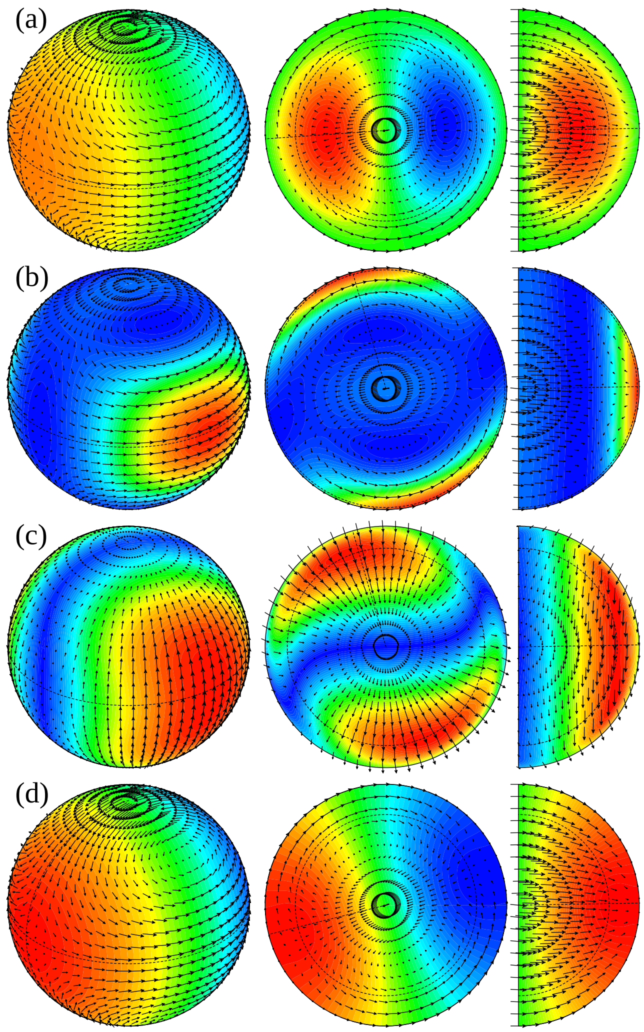

FIG. 10. (a) Contour plots of Θ and velocity field of the $m = 1$ mode for $\mathrm{Bi} = \infty$, $\mathrm{Pr} = 1.22 \times 10^{-2}$, $\mathrm{Ek} = 10^{-3}$, and $\mathrm{Ra} = 7969$. (b) Same as (a) but for the kinetic energy density. (c) Contour plots of the norm of the vorticity, and vorticity field for the same parameters. (d) Same as (a) but for $\mathrm{Bi} = 10^{-4}$, $\mathrm{Pr} = 2.80 \times 10^{-3}$, $\mathrm{Ek} = 10^{-3}$, and $\mathrm{Ra} = 2198$. The plots of K and the vorticity for the parameters of (d) are very similar to (b) and (c), respectively.

exterior when $\mathrm{Bi} \lesssim 10^2$.

- The range of parameters where the torsional oscillations are preferred at onset becomes smaller when the flux of heat released through the surface diminishes (compare the radial derivative of Θ in Figs. 6 and 7 near the boundary). However, it never strangles to an empty set, indicating that the existence of preferred torsional modes is independent of the boundary condition of the temperature.

- For a selected pair of parameters inside the bounds defined by Fig. 3, there is a critical Bi at which the torsional oscillations are superseded by ARWs of azimuthal wave number $m = 1$ or $m = 2$. From this point Ra_c becomes about three times lower than for $\mathrm{Bi} \gtrsim 10^2$.

- An adequate scaling of the nondimensional parameters shows the existence of a universal behavior of the bicritical curves for small Ek as seen in Figs. 3 and 4. It has been found that the ratio Pr/Ek for the appearance of the torsional solutions follows the law $\mathrm{Pr}/\mathrm{Ek} \sim 0.8/\mathrm{f}_{\mathrm{Pr}/\mathrm{Ek}}(\mathrm{Bi})$, the critical Rayleigh number goes as $\mathrm{Ra}_c \sim 0.85/\mathrm{f}_{\mathrm{Ra}}(\mathrm{Bi})$, and the critical frequencies as $\omega_{0,1} \sim 10\,\mathrm{Pr}^{-1}/\mathrm{g}_{\mathrm{Pr}}(\mathrm{Bi}) \sim 12.5\,\mathrm{Ek}^{-1}\,\mathrm{f}_{\mathrm{Pr}/\mathrm{Ek}}(\mathrm{Bi})/\mathrm{g}_{\mathrm{Pr}}(\mathrm{Bi})$, where the functions $\mathrm{f}_{\mathrm{Pr}/\mathrm{Ek}}$, f_{Ra}, and g_{Pr} are stated in Eq. (33), with the fitted values of the coefficients c and p given in the text. This suggests that an asymptotic analysis is possible including the Robin conditions for any value of Bi.

- The existence of a non-empty $m = 0$ region in the limit $\mathrm{Bi} \to 0$ supports the possible existence of torsional oscillations in Astrophysics even when the heat released to the exterior of a celestial body is not optimal.

ACKNOWLEDGMENTS

This research has been supported by the Spanish Ministry of Science and Innovation and the European Regional Development Fund, under Grant PID2021-125535NB-I00.

DATA AVAILABILITY STATEMENT

The data that support the findings of this study are available from the corresponding author upon reasonable request.

---

[1] S. A. Triana, G. Guerrero, A. Barik, and J. Rekier, "Identification of Inertial Modes in the Solar Convection Zone," Astrophys. J. Lett. **934:L4**, 9pp (2022).

[2] C. S. Hanson, S. Hanasoge, and K. R. Sreenivasan, "Discovery of high-frequency retrograde vorticity waves in the Sun," Nat. Astron. **6**, 708–714 (2022).

[3] K. Zhang, "On equatorially trapped boundary inertial waves," J. Fluid Mech. **248**, 203–217 (1993).

[4] K. Zhang, "On coupling between the Poincaré equation and the heat equation: non-slip boundary condition," J. Fluid Mech. **284**, 239–256 (1995).

[5] K. Zhang, X. Liao, and F.H. Busse, "Asymptotic solutions of convection in rapidly rotating non-slip spheres," J. Fluid Mech. **578**, 371–380 (2007).

[6] E. Dormy, A. M. Soward, C. A. Jones, D. Jault, and P. Cardin, "The onset of thermal convection in rotating spherical shells," J. Fluid Mech. **501**, 43–70 (2004).

[7] M. Net, F. Garcia, and J. Sánchez, "On the onset of low-Prandtl-number convection in rotating spherical shells: non-slip boundary conditions," J. Fluid Mech. **601**, 317–337 (2008).

[8] M. Ardes, F. H. Busse, and J. Wicht, "Thermal convection in rotating spherical shells," Phys. Earth Planet. Inter. **99**, 55–67 (1997).

[9] S. Liu, Z.-H. Wan, R. Yan, C. Sun, and D.-J. Sun, "Onset of fully compressible convection in a rapidly rotating spherical shell," J. Fluid Mech. **873**, 1090–1115 (2019).

[10] Y. Lin and A. Jackson, "Large-scale vortices and zonal flows in spherical rotating convection," J. Fluid Mech. **912**, A46 (2021).

[11] T. T. Clarté, N. Schaeffer, S. Labrosse, and J. Vidal, "The effects of a Robin boundary condition on thermal convection in a rotating spherical shell," J. Fluid Mech. **918**, A36 (2021).

[12] R. S. Long, J. E. Mound, C. J. Davies, and S. M. Tobias, "Scaling behaviour in spherical shell rotating convection with fixed-flux thermal boundary conditions," J. Fluid Mech. **889**, A7–1–34 (2020).

[13] C. J. Davies, D. Gubbins, and P. K. Jimack, "Convection in a rapidly rotating spherical shell with an imposed laterally varying thermal boundary condition," J. Fluid Mech. **641**, 335–358 (2009).

[14] F. Garcia, J. Sánchez, and M. Net, "Antisymmetric polar modes of thermal convection in rotating spherical fluid shells at high Taylor numbers," Phys. Rev. Lett. **101**, 194501 (2008).

[15] F. Garcia, F. R. N. Chambers, and A. L. Watts, "Onset of low Prandtl number thermal convection in thin spherical shells," Phys. Rev. Fluids **3**, 024801 (2018).

[16] F. Garcia, J. Sánchez, and M. Net, "Numerical simulations of high-Rayleigh-number convection in rotating spherical shells under laboratory conditions," Phys. Earth Planet. Inter. **230**, 28–44 (2014).

[17] K. Lam, D. Kong, and K. Zhang, "Nonlinear thermal inertial waves in rotating fluid spheres," Geophys. Astrophys. Fluid Dyn. **112**, 357–374 (2018).

[18] M. Landeau and J. Aubert, "Equatorially asymmetric convection inducing a hemispherical magnetic field in rotating spheres and implications for the past martian dynamo," Phys. Earth Planet. Inter. **185**, 61–73 (2011).

[19] R. Monville, J. Vidal, D. Cébron, and N. Schaeffer, "Rotating double-diffusive convection in stably stratified planetary cores," Geophys. J. Int. **219**, S195–S218 (2019).

[20] J. Sánchez Umbría and M. Net, "Thermal convection in rotating spherical geometry: A numerical overview of the transitions from periodic axisymmetric to temporally complex three-dimensional flows," Phys. Rev. E **106**, 065102 (2022).

[21] M. Net, F. Garcia, and J. Sánchez, "Numerical study of the onset of thermosolutal convection in rotating spherical shells," Phys. Fluids **24**, 064101–1–064101–21 (2012).

[22] J. Sánchez, F. Garcia, and M. Net, "Critical torsional modes of convection in rotating fluid spheres at high Taylor numbers," J. Fluid Mech. **791**, R1 (2016).

[23] K. Zhang, K. Lam, and D. Kong, "Asymptotic theory for torsional convection in rotating fluid spheres," J. Fluid Mech. **813**, R2 (2017).

[24] D. Kong, K. Zhang, K. Lam, and A. P. Willis, "Axially symmetric and latitudinally propagating nonlinear patterns in rotating spherical convection," Phys. Rev. E **98**, 031101(R) (2018).

[25] J. Sánchez Umbría and M. Net, "Torsional solutions of convection in rotating fluid spheres," Phys. Rev. Fluids **4**, 013501 (2019).

[26] J. Sánchez Umbría and M. Net, "Continuation of Double Hopf Points in Thermal Convection of Rotating Fluid Spheres," SIAM J. Appl. Dyn. Syst. **20**, 208–231 (2021).

[27] W. Li and D. Kong, "Rapidly rotating self-gravitating Boussinesq fluid. II. Onset of thermal inertial convection in oblate spheroidal cavities," Phys. Rev. Fluids **7**, 103502 (2022).

[28] W. Li and D. Kong, "Rapidly rotating self-gravitating Boussinesq fluid. III. A previously unknown zonal oscillation at the onset of rotating convection," Phys. Rev. Fluids **8**, L011501 (2023).

[29] L.S. Tuckerman and D. Barkley, "Bifurcation analysis of the Eckhaus instability," Physica D **46**, 57–86 (1990).

[30] M. Net and J. Sánchez Umbría, "Periodic orbits in tall laterally heated rectangular cavities," Phys. Rev. E **95**, 023102 (2017).

[31] J. Sánchez Umbría and M. Net, "Three-dimensional quasiperiodic torsional flows in rotating spherical fluids at very low Prandtl numbers," Phys. Fluids **33**, 114103 (2021).

[32] S. Chandrasekhar, *Hydrodynamic and Hydromagnetic Stability* (Oxford University Press, New York, 1961).

[33] J. Sánchez, F. Garcia, and M. Net, "Radial collocation methods for the onset of convection in rotating spheres," J. Comput. Phys. **308**, 273 – 288 (2016).

[34] T. Williams, C. Kelley, and et al., "Gnuplot 4.6: an interactive plotting program," `http://gnuplot.sourceforge.net/` (2013).